Acta Materialia 253 (2023) 118945

Contents lists available at ScienceDirect

Acta Materialia

journal homepage: www.elsevier.com/locate/actamat

Full length article

The three-dimensional elastodynamic solution for dislocation plasticity and its implementation in discrete dislocation dynamics simulations

Junjie Yang [a,*], Ali Rida [a], Yejun Gu [a,b], Daniel Magagnosc [c], Tamer A. Zaki [a], Jaafar A. El-Awady [a,*]

[a] Department of Mechanical Engineering, Whiting School of Engineering, Johns Hopkins University, Baltimore, MD, 21218, USA
[b] Institute of High Performance Computing (IHPC), Agency for Science, Technology and Research (A*STAR), Singapore, 138632, Singapore
[c] DEVCOM Army Research Laboratory, Army Research Directorate, Aberdeen Proving Ground, MD, 21005, USA

ARTICLE INFO

Keywords:
Dislocation dynamics
Elastodynamic solution
Stress waves
Boundary value problems

ABSTRACT

An analytical solution for the elastodynamic displacement field of non-uniformly moving Volterra dislocations is derived using the Green's function approach. The elastodynamics strain and stress fields can then be evaluated by numerically differentiating the displacement field. Qualitative comparisons are made with molecular dynamic simulations, and the analytical solution is shown to capture the same features. The plane waves that emanate from, and are parallel to, the slip plane during the instantaneous injection process of edge or screw dislocations are captured by the analytical solution. This was not captured by previously proposed elastodynamic solutions. A computationally efficient swept-area-tracking algorithm is then developed and implemented into three-dimensional discrete dislocation dynamics simulations to compute the elastodynamic field induced by dislocation movements and interactions. This approach provides a way forward for modeling deformation of materials under shock loading or quantifying the dynamics effects that dominate during dislocation avalanches during deformation of metals.

1. Introduction

A stationary dislocation in a material induces a static elastic stress field due to the distortion of atoms from their ideal locations at and near the dislocation. As dislocations glide due to the presence of an external field (e.g., applied thermal–mechanical or electric fields) or due to local high internal stresses induced by other defects in the material, the local rearrangements of the atoms will induce dynamic elastic waves (stress, strain, and displacement waves) that are emitted from the dislocation. These waves propagate at the transverse/longitudinal speed of sound in the material, which is on the order of $\sim$ 1 km/s in metals. When the dislocation velocity is considerably smaller than this wave speed, the evolution of the elastic field waves can be assumed to happen instantaneously and the atomic displacement and stress states can be assumed to have quasi-static evolution. This is a common assumption for most existing discrete dislocation dynamics (DDD) simulations (e.g., [1–5]). However, since the quasi-static approximation neglects the interaction between the dynamic elastic field and dislocations moving at speeds on the same order of the transverse/longitudinal speed of sound, this approximation can lead to significant errors. An example is manifested in spurious dislocation nucleation observed in front of a stress wave that is induced by shock loading when using the quasi-static assumption [6]. Furthermore, the quasi-static solution is oversimplified for describing key phenomena of dislocation avalanches, during which dislocation velocities can be on the order of the transverse/longitudinal speed of sound [7].

The dynamic elastic field of moving dislocations was analytically derived in 1963 by Mura [8]. This analytical elastodynamic solution is complex due to the coupled spatial–temporal integration, so this solution has not been feasible to be numerically evaluated within the framework of DDD simulations. On the other hand, Markenscoff derived the explicit elastodynamic fields for infinitely straight screw and edge dislocations as well as for dislocation loops [9–11]. These solutions were restricted to simple dislocation geometries. Building on these solutions, Gurrutxaga implemented the first time-dependent two-dimensional (2D) dislocation dynamics plasticity model [6,12]. However, due to the 2D treatment, the capability of this model is limited to plane problems. Recently, Cui et al. [13] used the retarded potentials technique to simplify the coupled spatial–temporal integral [8] to merely a spatial integral over the retarded positions of dislocation segments. This enabled the development of a computational procedure for computing the elastodynamic stress fields of three-dimensional

* Corresponding authors.
E-mail addresses: junjie.yang@jhu.edu (J. Yang), jelawady@jhu.edu (J.A. El-Awady).

https://doi.org/10.1016/j.actamat.2023.118945
Received 31 January 2023; Received in revised form 11 April 2023; Accepted 12 April 2023
Available online 17 April 2023

(3D) dislocations [13]. This procedure is based on a segment-based algorithm, where dislocations are discretized into connected segments. Nevertheless, this algorithm would encounter computational challenges when modeling complex dislocation networks where multiple dislocations collide and annihilate, since tremendous numerical efforts would be needed to track the changes of the integral path due to the changes of the connectivity between segments. Additionally, this model is only capable of evaluating the stress field in an infinite medium. To solve a complete boundary-value problems (BVP), both the displacement field and stress field are required [14].

Here, the full 3D elastodynamic field for Volterra dislocations is derived using the Green's function approach. This field is then validated by comparisons with molecular dynamics (MD) simulations of injected edge and screw dislocations. The elastodynamic displacement solution is then implemented in a 3D DDD framework. This computational procedure can be easily coupled with the boundary element method [15] or the finite element method [16] to resolve the elastodynamic BVPs.

2. Methodologies

2.1. Theoretical derivation of the 3D elastodynamic displacement field

In continuum mechanics, the elastodynamic equilibrium equations in the absence of body forces are:

$$\sigma_{ij,j}(\mathbf{x},t) = \rho \ddot{u}_i(\mathbf{x},t) \tag{1}$$

where the stress tensor, $\boldsymbol{\sigma} = \sigma_{ij}$, and the displacement vector, $\mathbf{u} = u_i$, are both a function of time, t, and space, $\mathbf{x} = x_i$, while the material density, ρ, is assumed isotropic and independent of time. Additionally, the displacement gradient, $u_{i,j}$, can be assumed to be the superposition of the elastic distortion, β^E_{ij}, and the plastic distortion, β^P_{ij}, such that [8,13]:

$$u_{i,j} = \beta^E_{ij} + \beta^P_{ij} \tag{2}$$

Thus, the linear elastic constitutive law becomes:

$$\sigma_{ij} = C_{ijkl}\beta^E_{k,l} \tag{3}$$

where C_{ijkl} is the elastic modulus tensor, which for isotropic material properties is given by: $C_{ijkl} = \lambda\delta_{ij}\delta_{kl} + \mu(\delta_{ik}\delta_{jl} + \delta_{il}\delta_{jk})$, with λ and μ being the Lamé's first parameter and shear modulus, respectively.

From Eqs. (1) through (3), the elastic displacement wave equation can be expressed as [17,18]:

$$(C_{ijkl}\partial_l\partial_j - \rho\delta_{ik}\partial_t^2)u_k = C_{ijkl}\beta^P_{kl,j} \tag{4}$$

where δ_{ik} is the Kronecker delta. By defining the differential operator in Eq. (4) as $L_{ik} = C_{ijkl}\partial_l\partial_j - \rho\delta_{ik}\partial_t^2$, the impulse response of an inhomogeneous linear differential equation, should satisfy the following relationship [13,18]:

$$L_{ik}G_{km}(\mathbf{x},t;\mathbf{x}',t') = \delta_{im}\delta(\mathbf{x}-\mathbf{x}')\delta(t-t') \tag{5}$$

where $\delta()$ is the Dirac delta function, $\mathbf{x}'$ is the point impulse position vector, and t' is the time of the impulse. Thus, the elastodynamic displacement field can be expressed using a spatial–temporal convolution as:

$$u_k(\mathbf{x},t) = C_{mnpq}G_{km}(\mathbf{x},t;\mathbf{x}',t') * \beta^P_{pq,n}(\mathbf{x},t) \tag{6}$$

or alternatively:

$$u_k(\mathbf{x},t) = C_{mnpq}G_{km,n}(\mathbf{x},t;\mathbf{x}',t') * \beta^P_{pq}(\mathbf{x},t) \tag{7}$$

where $*$ denotes the spatial–temporal convolution.

By expressing the plastic distortion resulting from the slip of a single dislocation loop with Burgers vector $\mathbf{b} = b_i$ as [13,19]:

$$\beta^P_{ij}(\mathbf{x},t) = -\iint_{S(t)} \delta(\mathbf{x}-\mathbf{s})b_i n_j dS \tag{8}$$

where $S(t)$ is the surface swept by the dislocation at time t, and $\mathbf{n} = n_i$ is the unit normal vector to the swept surface, the solution of Eq. (7) becomes (see full derivation in supplementary materials Section S1):

$$\begin{aligned}
\mathbf{u}(\mathbf{x},t) = {} & \frac{1}{4\pi}\iint_{S|_{t-t'=\frac{r}{c_T}}} \frac{1}{r^3}\left[\frac{12\mathbf{r}(\mathbf{b}\cdot\mathbf{r})(\mathbf{n}\cdot\mathbf{r})}{r^2} - 3\mathbf{b}(\mathbf{n}\cdot\mathbf{r}) - 3\mathbf{n}(\mathbf{b}\cdot\mathbf{r})\right. \\
& \left. - 2\mathbf{r}(\mathbf{b}\cdot\mathbf{n})\right] dS' \\
& - \frac{1}{4\pi c_T}\frac{\partial}{\partial t}\iint_{S|_{t-t'=\frac{r}{c_T}}} \frac{1}{r^2}\left[\mathbf{b}(\mathbf{r}\cdot\mathbf{n}) + \mathbf{n}(\mathbf{r}\cdot\mathbf{b}) - 2\frac{\mathbf{r}(\mathbf{r}\cdot\mathbf{b})(\mathbf{r}\cdot\mathbf{n})}{r^2}\right] dS' \\
& + \frac{(1-2\nu)}{4\pi(1-\nu)}\iint_{S|_{t-t'=\frac{r}{c_L}}} \frac{1}{r^3}\left[\frac{1-3\nu}{1-2\nu}\mathbf{r}(\mathbf{b}\cdot\mathbf{n}) + \mathbf{b}(\mathbf{r}\cdot\mathbf{n}) + \mathbf{n}(\mathbf{r}\cdot\mathbf{b})\right. \\
& \left. - 6\frac{\mathbf{r}(\mathbf{r}\cdot\mathbf{b})(\mathbf{r}\cdot\mathbf{n})}{r^2}\right] dS' \\
& - \frac{(1-2\nu)}{4\pi c_L(1-\nu)}\frac{\partial}{\partial t}\iint_{S|_{t-t'=\frac{r}{c_L}}} \frac{1}{r^2}\left[\frac{\nu}{1-2\nu}\mathbf{r}(\mathbf{b}\cdot\mathbf{n}) + \frac{\mathbf{r}(\mathbf{b}\cdot\mathbf{r})(\mathbf{r}\cdot\mathbf{n})}{r^2}\right] dS' \\
& + \frac{3c_T^2}{2\pi}\int_{1/c_L}^{1/c_T}\iint_{S|_{t-t'=\kappa r}} \frac{\kappa}{r^3}\left[\mathbf{b}(\mathbf{n}\cdot\mathbf{r}) + \mathbf{r}(\mathbf{b}\cdot\mathbf{n}) + \mathbf{n}(\mathbf{b}\cdot\mathbf{r})\right. \\
& \left. - \frac{5\mathbf{r}(\mathbf{b}\cdot\mathbf{r})(\mathbf{n}\cdot\mathbf{r})}{r^2}\right] dS' d\kappa
\end{aligned} \tag{9}$$

Here, c_T and c_L are the transverse and longitudinal wave speeds in the isotropic material, ν is the Poisson's ratio, $\mathbf{r} = \mathbf{x} - \mathbf{x}'$ is the vector pointing from the integration point $\mathbf{x}'$ to the field point $\mathbf{x}$ at which the displacement vector $\mathbf{u}$ is to be calculated, r is the magnitude of $\mathbf{r}$, and t' is the time when the integration point $\mathbf{x}'$ is swept by a dislocation. The surface integral in Eq. (9) represents the integration over all the swept areas for which their associated elastic waves have reached the observer, as shown schematically in Fig. 1(a) . Additionally, the first and second terms on the right hand side of Eq. (9) represent the contribution from the transverse wave, while the third and fourth terms represent the contribution from the longitudinal wave. Finally, the last term is a cross-contribution term from both the transverse and the longitudinal waves. The long-time limit of Eq. (9) is shown to converge to the classic static solution, as discussed in Section S1 of the supplementary materials.

Finally, in the framework of the infinitesimal strain theory, the components of the strain tensor at any point in space and time are computed from $\varepsilon_{ij} = 1/2\left(u_{i,j} + u_{j,i}\right)$ and those for the stress tensor are computed from $\sigma_{ij} = \lambda u_{k,k}\delta_{ij} + \mu(u_{i,j} + u_{j,i})$.

2.2. Implementation of the elastodynamic field in 3D discrete dislocation dynamics simulations

The main challenge in calculating the elastodynamic displacements using Eq. (9) in the framework of 3D DDD simulations is determining the integral surface $S|_{t-t'=\frac{r}{c}}$. For this purpose, we have developed a scalable algorithm to numerically implement Eq. (9) into 3D DDD simulations. The details and a schematic representation of the numerical algorithm are provided in Section S3 of the supplementary materials. This implementation and all simulations here are conducted using a significantly modified in-house version of the 3D DDD open-source code ParaDiS [4]. These modifications include avoiding all artificial non-planar dislocation glide or collision events for dislocation slip in FCC crystals, incorporating atomistically-informed cross-slip mechanisms, and accounting for free-surfaces, as described in [20,21]. In this code, dislocations are discretized into linear segments connected at dislocation nodes, which provides a direct way to discretize the swept area as the dislocation glides on its primary slip plane (or cross-slip to another plane). As a dislocation segment glides in one time step to a new position, the initial and final positions of the end nodes of the dislocation segment represent the corners of a quadrilateral element that defines the discretized swept area. This is shown schematically in Fig. 1(b). For each quadrilateral element, four parameters are stored for use when numerically solving Eq. (9): the elementary area vector, $\mathbf{dS}'$;

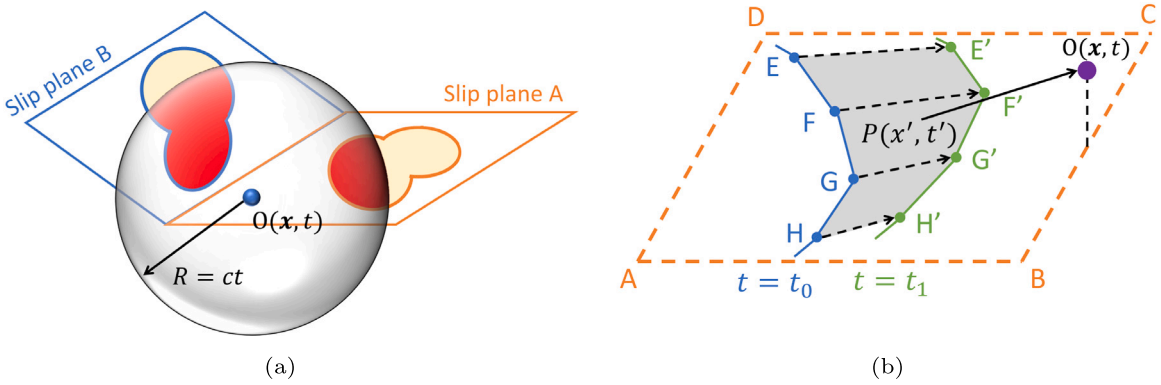

Fig. 1. (a) Schematic showing two dislocation loops colored according to their slip plane at time t. The two loops are assumed to nucleate at time $t' = 0$. The translucent 3D sphere is the view field of the observer $O(\mathbf{x}, t)$ at its center, who is located at $\mathbf{x}$ at time t with respect to the time when the loops nucleated. The areas shown in red represent the swept areas for which their associated elastic waves have reached the observer at time t, while the waves of the swept areas shown in yellow have not reached the observer yet (i.e., they are not included in the surface integral at time t). (b) Schematic of the automatic discretization of an area swept by dislocation segments in the 3D DDD framework. The section of the dislocation loop initially at time $t = t_0$ is discretized into linear segments connected at dislocation nodes E, F, G, and H. After one time step ($t = t_1$), the dislocation glides on plane ABCD and the new positions of the dislocation nodes become E', F', G', and H'. The new and old positions of the dislocation nodes represent the corners of quadrilateral elements, for example FGG'F', that define the discretized swept area. (For interpretation of the references to color in this figure legend, the reader is referred to the web version of this article.)

the position of the swept area, $\mathbf{x}'$, which is represented by the centroid of the area; the time when the area is swept, which is approximated by the average between t_0 and t_1; and the burgers vector, $\mathbf{b}$, of the dislocation segment that swept that area.

The elastodynamic displacements as defined by Eq. (9) can then be computed numerically for any "observer" as follows. At every time step the distances between the observer and the centroid of each quadrilateral is computed. The contribution, according to Eq. (9), of all elements that satisfy the condition $t - t' \leq r/c$ are then summed to evaluate $\mathbf{u}(\mathbf{x}, \mathbf{t})$. For each swept quadrilateral element, their parameters will be removed from the computer memory once the furthest point in the simulation box receives the slowest elastic wave. The time derivatives in the second and fourth terms in Eq. (9) are approximated using forward difference. The distortion tensor $u_{i,j}$ is also calculated by the forward difference of the elastodynamic displacement field $\mathbf{u}(t)$, from which the strain and stress tensors can be computed as previously discussed.

3. Molecular dynamics simulations setup

To validate the elastodynamics field given by Eq. (9) and its implementation into 3D DDD simulations the displacement and stress fields emitted from an infinitely long and straight screw or edge dislocation can be compared to those calculated using molecular dynamics (MD) simulations of an infinitely long dislocation injected into an all-atom simulation cell. All MD simulations are conducted using the open source Large-scale Atomic/Molecular Massively Parallel Simulator (LAMMPS) [22], with the embedded atom method (EAM) interatomic potential developed by Mishin et al. for Al [23]. Al is chosen here for its isotropic elastic response (i.e., $2C_{44}/\left(C_{11} - C_{12}\right) = 1.2$), which makes it suitable for comparison with the derived isotropic elastodynamic solution developed earlier. This EAM potential was also shown to accurately reproduce the basic equilibrium properties of pure FCC Al, including, the elastic constants, the phonon-dispersion curves, the vacancy formation and migration energies, the stacking fault energies, and the surface energies [23]. The material parameters predicted by this potential and also used in the 3D DDD simulations are summarized in Table 1.

The injection of an infinitely long straight screw dislocation is simulated in MD by first constructing a rectangular simulation cell having dimensions $60\sqrt{6}a_0 \times 86\sqrt{3}a_0 \times 20\sqrt{2}a_0$, where a_0 is the lattice parameter. Thus, the simulation cell has a total of 2,489,880 atoms. The edges of the simulation cell are parallel to the $x = [112]$, $y = [\bar{1}\bar{1}1]$, and $z = [1\bar{1}0]$ directions, respectively, and the origin is defined at the center of the simulation box. Periodic boundary conditions are then imposed along the z direction, while free surfaces boundary conditions were imposed along the x, and y directions, respectively. The simulation cell was then relaxed at 0.5 K using a Langevin thermostat in the microcanonical ensemble (i.e., NVE ensemble) for 5 ps to ensure that all the components of the pressure tensor on both free surfaces are zero. The time step used in all subsequent simulations is $\Delta t = 1$ fs. A $1/2[1\bar{1}0]$ screw dislocation was then injected at the center of the simulation cell over a time-span of $\tau = 1$ ps as follows. First, a cut plane is identified midway between two $(\bar{1}\bar{1}1)$ planes as shown in Fig. 2(a) and all atoms having $x < 0$ in the $(\bar{1}\bar{1}1)$ plane just above ($y > 0$) and below ($y < 0$) this cut plane were selected. The atoms above the cut were then displaced by $u_z = -\frac{bt}{2\tau}$, and the atoms below by $u_z = \frac{bt}{2\tau}$ from $t = 0$ to 1 ps, where t is the simulation time. Finally, the positions of the displaced atoms are fixed and all other atoms are allowed to dynamically relax the stacking fault induced by the imposed displacement field.

Table 1
Material properties as predicted by the EAM potential and used in the 3D DDD simulations.

ν	μ	b	Density	Lattice parameter a_0
0.35	26.2 GPa	0.2864 nm	2700 kg/m^3	4.05 Å

The displacement of the atoms above and below the cut plane will generate a stacking fault ribbon surrounded by two partials. The leading partial will first nucleate at the center of the simulation cell and then the trailing partial will form from the free surface when the displacement difference between the atoms above and below the cut plan is equal to b. An extended screw dislocation will then form at the center of the simulation cell. This process leads to a sudden rise in the temperature of the system by ~ 1 K, which is then relaxed by the Langevin thermostat. For time $t > 1$ ps the simulation cell is relaxed at 0.5 K, during which, the displacement wave will propagate through the simulation volume.

For the MD simulations of the injection of a $1/2[1\bar{1}0]$ edge dislocation on the (111) plane in pure FCC Al, a rectangular simulation cell is first constructed with edge length $140\sqrt{2}a_0 \times 116\sqrt{3}a_0 \times 10\sqrt{6}a_0$ (i.e, a total of 3,915,780 atoms). The edges of the simulation cell are parallel to the $x = [1\bar{1}0]$, $y = [111]$, and $z = [\bar{1}\bar{1}2]$ direction, respectively. Periodic boundary conditions are imposed along the $z = [\bar{1}\bar{1}2]$ direction, while free surfaces boundary conditions are imposed along the $x = [1\bar{1}0]$, and $y = [111]$ directions. The origin is chosen at the center of

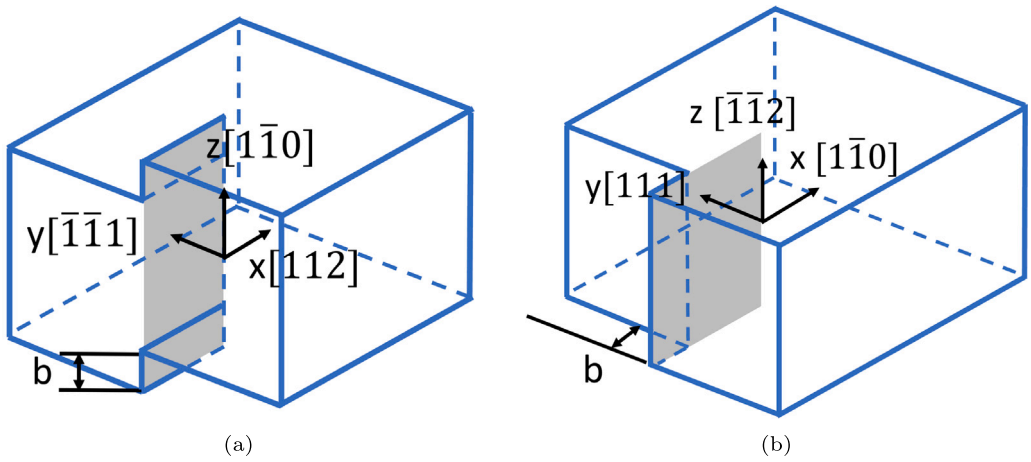

Fig. 2. Schematic representation of the initial conditions to inject a straight (a) screw dislocation; and (b) edge dislocation in a perfect crystal in both the elastodynamic model and MD simulations.

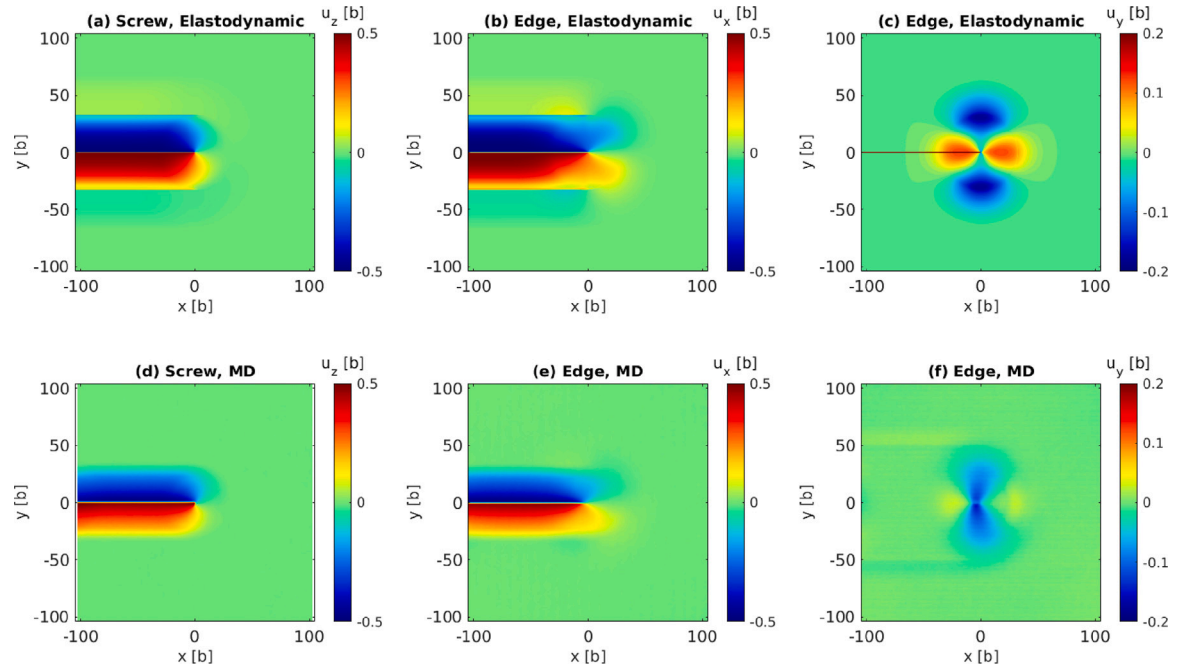

Fig. 3. The nonzero elastodynamic displacement components computed from Eq. (9) for an instantaneously injected infinitely long straight: (a) screw; and (b)–(c) edge dislocation. The nonzero elastodynamics displacement field predicted from MD simulations for an instantaneously injected infinitely long straight: (d) screw; and (e)–(f) edge dislocation. All results are shown after 3 ps from the moment the dislocation was injected.

the simulation cell. The simulation cell is then first relaxed at 0.5K in NVE ensemble for 5 ps. A cut plane is identified midway between two (111) planes as shown in Fig. 2(b). Two (1$\bar{1}$0) planes above the cut ($y > 0$) were then deleted, followed by the same injection process applied for the screw dislocation simulations, except that the imposed atom displacements in this case are in the x direction with $u_x = -\frac{bt}{2\tau}$ for the atoms above the cut ($y > 0$) and $u_x = \frac{bt}{2\tau}$ for the atoms below the cut ($y < 0$).

4. Results and discussion

Fig. 3 shows a comparison between the elastodynamics displacements as computed from Eq. (9) and those from the MD simulations for the cases of instantaneously injected screw and edge dislocations. The stress fields, obtained by differentiating the displacement fields, are also shown in Fig. 4.

For the elastodynamic solution using Eq. (9), an infinitely long screw or edge dislocation was introduced parallel to the simulation cell z-axis with a cut plane in the negative xz-plane, as shown schematically in Fig. 2. The initial conditions for the injection of the screw dislocation are:

$$\begin{cases} u_z(t=0, x<0, y=0^+, z) = b/2 \\ u_z(t=0, x<0, y=0^-, z) = -b/2 \end{cases} \tag{10}$$

where u_z is the z component of the displacement vector. On the other hand, the initial conditions for the injection of the edge dislocation are:

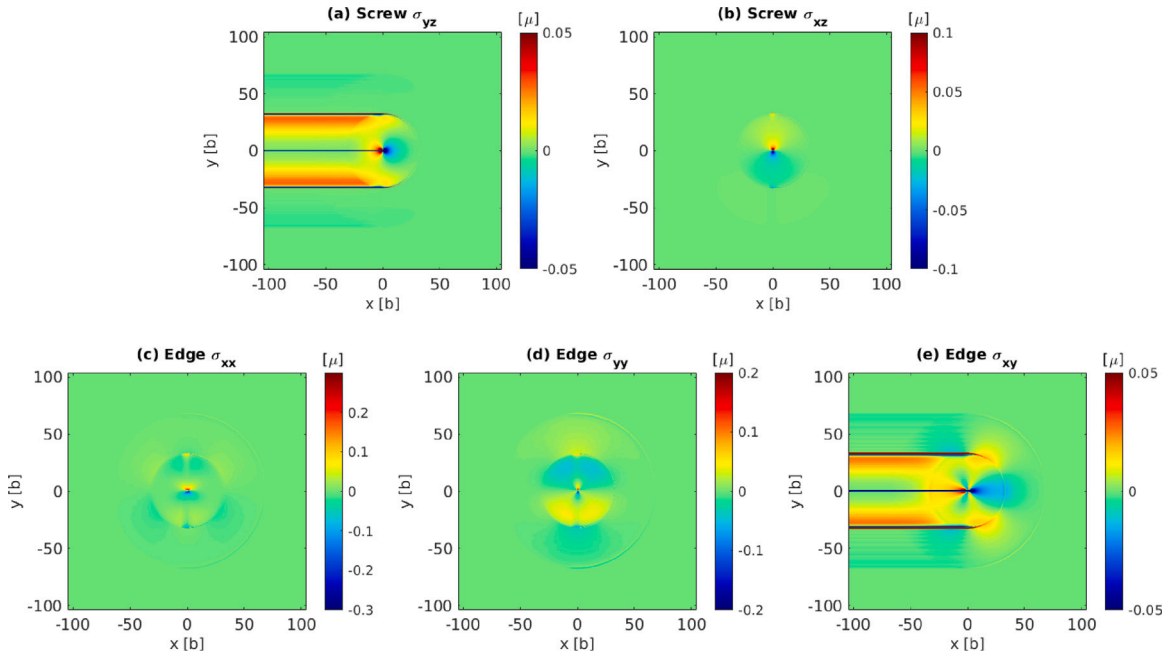

Fig. 4. The nonzero elastodynamic stress components computed from Eq. (9) for an instantaneously injected infinitely long straight: (a)–(b) screw; and (c)–(e) edge dislocation. All results are shown after 3 ps from the moment the dislocation was injected.

$$\begin{cases} u_x(t=0, x<0, y=0^+, z) = b/2 \\ u_x(t=0, x<0, y=0^-, z) = -b/2 \end{cases} \tag{11}$$

where u_x is the x component of the displacement vector. In both the screw and edge dislocation cases, the entire cut plane is assumed to be disturbed instantaneously at $t = 0$. Thus, every point on the cut plane would be a source emanating an elastic waves starting at time $t = 0$.

As shown in Fig. 3, the displacement fields for both the screw and edge dislocations as computed from Eq. (9) and from the MD simulations are in good agreement. In particular, it is observed that for the screw dislocation the u_z component is the superposition of a cylindrical wave that emits from the dislocation line and two transverse plane waves that propagate from and parallel to the cut plane. The predicted transverse wave speed from the solution of Eq. (9) is $\sim$ 3050 m/s, which is in good agreement with that predicted from the MD simulations ($\sim 3120 \pm 100$ m/s).

Similar observations are made for the case of the edge dislocation. However, in this case, u_x and σ_{xy} show two plane waves. A faster longitudinal wave and a slower transverse wave. The longitudinal wave is not as obvious in the MD simulation due to the gradual injection process of the dislocation over a time span of 1 ps, whereas the calculations from Eq. (9) using the initial conditions in Eq. (11) assume an instantaneous injection process. The longitudinal waves are more evident in the σ_{xy} contour shown in Section S2 of the supplementary material.

It should be noted that in previous 2D and 3D theoretical derivations of the elastodynamics field [6,13], the planar waves induced by the instantaneous injection process were missing, yet observed in the current simulations. This can be attributed to the following. In the 3D elastodynamic stress equation derived by Cui et al. [13], the stresses are computed as a line integral along the retarded position of dislocations. This integral is path dependent (i.e., depends on the entire history of positions of all dislocations over time). Thus, for the case of an instantaneous dislocation injection in the middle of the simulation volume using the solution developed by [13], there is no defined path for the dislocation to be placed at the center of the simulation cell. Therefore, the solution of Cui et al. [13] predicts the elastic wave emitted from the location of the final position of the dislocation line that was instantaneously injected and ignores the contribution from the half plane instantaneously swept by the injected dislocation. Thus, the solution in [13] misses the causality between the swept area of the injected dislocation and the generated plane waves.

Verschueren et al. observed the same plane wave emission in their MD simulations of instantaneously injected dislocations and they have analyzed the different ways the injection process affects these wave fronts. They then attempted to correct their prior 2D elastodynamic solutions, which did not predict these waves [6], by adding the contribution from the pole that was previously ignored in their integral. However, their corrections did not really match their MD results. Their corrected elastodynamic solution results in a constant planar displacement wave that had no contribution to the stress wave. Thus, unlike the MD simulations, their stress wave predictions did not show any planar wave. Additionally, their 2D elastodynamic solution showed an abrupt transition from the cylindrical wave front into the constant planar waves, which was not something observed in the MD simulations. They suggested that these differences between their MD simulations and proposed 2D elastodynamic solution are from artificial simplifications of the injection process in the continuum. However, our current 3D elastodynamic solution shows more accurate comparison with the MD simulations in both the displacement and stress waves produced. It is also shown in our solution that the variation of u_z along the y axis naturally produces the two transverse planar waves that they attributed to the artifacts in the injection process.

Finally, it should be noted that the calculated wave fronts from Eq. (9) are much sharper than those observed in the MD simulations. Verschueren et al. [24] have shown that the gradual injection process and the finite width of dislocation cores in MD simulations partially explain the smoother waves and the in-plane displacement components in MD predictions compared to continuum injection. The comparisons between our elastodynamic solution and MD simulations are supportive of their analysis. This is because the displacement boundary conditions in the MD simulations are gradually increased over a time period of 1 ps, while in the solution from Eq. (9) the dislocations are injected instantaneously. Thus, the intensity of the wave fronts are smeared out by the gradual injection process in the MD simulations. Additionally, the u_y field of the edge dislocation in Fig. 3(f) from the MD simulation is observed to be weaker than that of the elastodynamic solution in

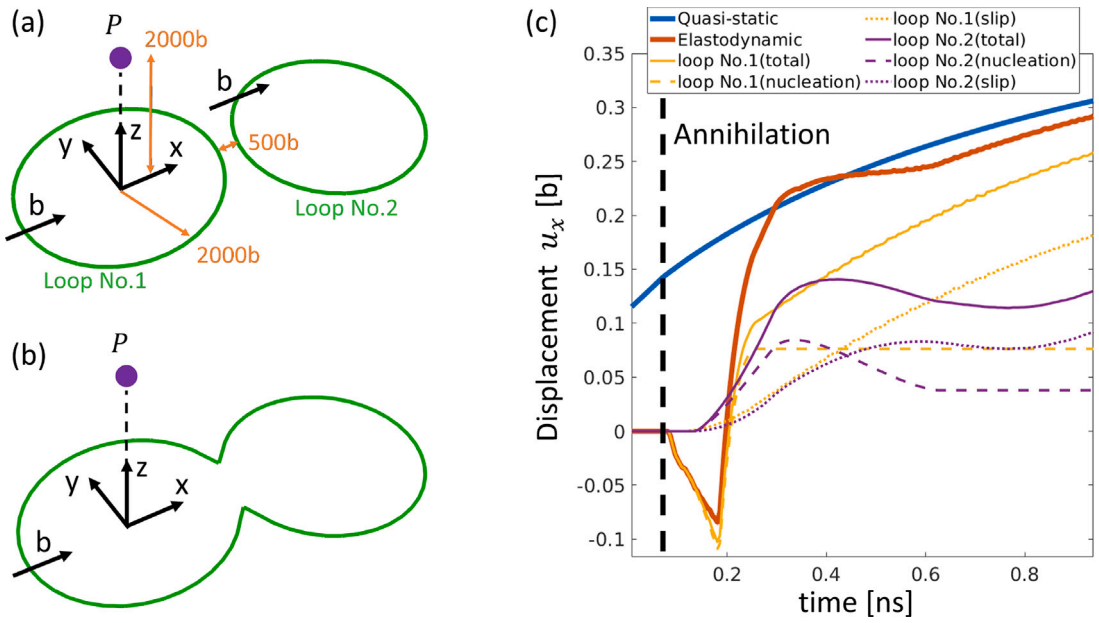

Fig. 5. The coalescence of two identical dislocation loops on the same slip plane. (a) Initial dislocation configuration. (b) Dislocation configuration at $t = 0.08$ ns, right after the coalescence. In (a) and (b) the x, y and z coordinates are in the $[01\bar{1}]$, $[111]$ and $[2\bar{1}\bar{1}]$ crystallographic directions, respectively. The Burgers vector of each loop is along the x direction. P represents the location of the observer. (c) The x component of the displacement at the observer P for the elastodynamic problem of both loop combined or each separately, as well as that for the quasi-static problem.

Fig. 3(c) because the current 3D elastodynamic model does not account for the dissociation of the edge dislocation that is naturally generated in Al due to energy minimization. The mathematical singularities along the slip plane and the dislocation line, as can be seen from the displacement field in Fig. 3(c) and resultant stress fields in Fig. 4(a, e), originates from the definition of the plastic distortion tensor defined in Eq. (8). Cutoff approximations are common in the realm of 3D DDD simulations to avoid such singularities in the absence of non-singular solutions (cf. [25–28] for the implementation of quasi-static stresses and Cui et al. [13] for the implementation of elastodynamic stress equations). In the quasi-static case, a non-singular solution [29] was previously developed and implemented in ParaDis [4]. Developing a non-singular solution for the elastodynamic solution is beyond the scope of the current work and further studies are required to develop a non-singular solution for elastodynamic field. Thus, here, the singularities in the derived elastodynamic solution is removed by using a cut-off distance a. If the point of interest is at a smaller distance to the dislocation than this distance then the singularity in the solution is avoided by replacing the smaller distance with a.

As a test case of the implementation of the current elastodynamic field within the framework of 3D DDD simulations, the elastodynamic interaction and annihilation of two co-planer dislocation loops in Al are also studied. The simulation parameters are shown in Table 1. Two identical dislocation loops are instantaneously introduced into an infinite simulation volume, as shown in Fig. 5(a). The initial radius of both loops is $2000b$ and the initial distance between their centers is $4500b$. A constant applied shear stress equal to 980 MPa is then applied to expand both loops. The elastodynamic stresses on each dislocation node are calculated every time step using Eq. (9). Fig. 5(b) shows the configuration of both loops after coalescing into a larger loop. The elastodynamic displacements as a function of time were also computed at a point "P" with position vector $(0, 2000b, 0)$, as shown in Fig. 5. Several physical processes are involved during this simulation, including dislocation loop injection, dislocation glide, and dislocation segments annihilation. To investigate the contributions from each process, both loops were also simulated independently with the same initial conditions, positions, and the same applied stress. The elastodynamic displacement curves for these cases are also shown in Fig. 5(c). A conventional DDD simulation, which assumes infinitely fast elastic wave speeds (i.e., quasi-static simulations), is also performed with the same applied stress for comparison.

By comparing the elastodynamic displacement and the quasi-static displacement curves in Fig. 5, it is observed that in the elastodynamics case, there is a delay before the observer at point P is able to detect the injection of either dislocation loop. On the other hand, in the quasi-static solution the same observer instantaneously detects the injected dislocation loops, as indicated by the finite displacement at time $t = 0$. Furthermore, in the elastodynamic solution, the observer will detect a dip in the displacement field between 0.1 and 0.2 ns due to the arrival of the waves induced by the injection of the first loop at time 0. Then at around 0.4 ns, the elastodynamic displacement overshoots the quasi-static displacement. This overshoot is the influence of the waves associated with the second injected loop finally reaching the observer. Eventually, both the elastodynamic and quasi-static curves will converge to a value of $0.5b$ when the entire plane below the observer has been swept. This example shows the capability of the algorithm to handle dislocation topological changes and the significance of considering elastodynamic effects for dislocations with high speed.

It should be noted that during dislocation avalanches, many dislocation activities, like nucleation and annihilation shown in this example happen collectively. Thus, it would be expected that the prominent difference between the elastodynamic and static solutions will be significantly amplified. Additionally, the dislocation speed in the current simulation is $\sim$ 450 m/s. It will be expected that the differences between the elastodynamic and quasi-static solutions will be even more obvious for dislocations moving at higher speeds, which is common in dislocation avalanches [7].

5. Conclusions

In conclusion, the 3D elastodynamic displacement field for Volterra dislocations was obtained using the Green's function approach. The elastodynamic stress field was then obtained by numerical differentiation of the displacement field. Thus, providing a complete solution for elastodynamic boundary value problems. The predictions from the current solution are in good agreement with those from MD simulations

in the following aspects. First, the current solution reproduces the same number of waves fronts and the same wave front velocities. Second, the commonly missed plane waves emitting parallel to the slip plane when a dislocation is injected into a simulation are correctly captured. Third, the predicted displacement and stress fields versus time are in good agreement with those predicted from the MD simulations. A scalable algorithm was also designed to numerically implement our elastodynamic solution into DDD simulations. The algorithm is robust to complex dislocation structures and interactions. This framework can be easily coupled with FEM simulations using the principle of superposition to solve 3D BVPs.

Declaration of competing interest

The authors declare that they have no known competing financial interests or personal relationships that could have appeared to influence the work reported in this paper.

Acknowledgments

The authors acknowledge helpful discussions with Prof. Giacomo Po (U. Miami) on the derivation of the elastodynamic solution, as well as discussions with Dr. Beñat Gurrutxaga-Lerma (U. Birmingham) on the planar wave fronts. This research was sponsored by the DEVCOM Army Research Laboratory, United States under Cooperative Agreement Number W911NF-20-2-0281. The authors also acknowledge support from the U.S. National Science Foundation (Grant No. 2225675). AR and JAE also acknowledge financial support by the Multiscale Structural Mechanics and Prognosis program at the Air Force Office of Scientific Research, United States (project number: FA9550-21-1-0028). YG acknowledges financial support by the Structural Metal Alloys Program (Grant No. A18B1b0061) of A*STAR in Singapore. The views and conclusions contained in this document are those of the authors and should not be interpreted as representing the official policies, either expressed or implied, of the DEVCOM Army Research Laboratory or the U.S. Government. The U.S. Government is authorized to reproduce and distribute reprints for Government purposes notwithstanding any copyright notation herein.

Appendix A. Supplementary data

Supplementary material related to this article can be found online at https://doi.org/10.1016/j.actamat.2023.118945.

References

[1] B. Devincre, L. Kubin, Mesoscopic simulations of dislocations and plasticity, Mater. Sci. Eng. A 234–236 (1997) 8–14, http://dx.doi.org/10.1016/S0921-5093(97)00146-9.

[2] N.M. Ghoniem, S.H. Tong, L.Z. Sun, Parametric dislocation dynamics: A thermodynamics-based approach to investigations of mesoscopic plastic deformation, Phys. Rev. B 61 (2) (2000) 913–927, http://dx.doi.org/10.1103/PhysRevB.61.913.

[3] D. Weygand, L.H. Friedman, E.V. der Giessen, A. Needleman, Aspects of boundary-value problem solutions with three-dimensional dislocation dynamics, Modelling Simul. Mater. Sci. Eng. 10 (4) (2002) 437, http://dx.doi.org/10.1088/0965-0393/10/4/306.

[4] A. Arsenlis, W. Cai, M. Tang, M. Rhee, T. Oppelstrup, G. Hommes, T.G. Pierce, V.V. Bulatov, Enabling strain hardening simulations with dislocation dynamics, Modelling Simul. Mater. Sci. Eng. 15 (6) (2007) 553.

[5] M. Fivel, C. Depres, An easy implementation of displacement calculations in 3D discrete dislocation dynamics codes, Phil. Mag. 94 (28) (2014) 3206–3214, http://dx.doi.org/10.1080/14786435.2014.949326.

[6] B. Gurrutxaga-Lerma, D.S. Balint, D. Dini, D.E. Eakins, A.P. Sutton, A dynamic discrete dislocation plasticity method for the simulation of plastic relaxation under shock loading, Proc. R. Soc. A: Math. Phys. Eng. Sci. 469 (2156) (2013) 20130141.

[7] P.D. Ispánovity, I. Groma, G. Györgyi, F.F. Csikor, D. Weygand, Submicron plasticity: Yield stress, dislocation avalanches, and velocity distribution, Phys. Rev. Lett. 105 (8) (2010) 085503.

[8] T. Mura, Continuous distribution of moving dislocations, Phil. Mag. 8 (89) (1963) 843–857.

[9] X. Markenscoff, The transient motion of a nonuniformly moving dislocation, J. Elasticity 10 (2) (1980) 193–201.

[10] X. Markenscoff, R. Clifton, The nonuniformly moving edge dislocation, J. Mech. Phys. Solids 29 (3) (1981) 253–262.

[11] X. Markenscoff, L. Ni, The singular nature of the stress field near an arbitrarily moving dislocation loop, J. Mech. Phys. Solids 38 (4) (1990) 481–490.

[12] B. Gurrutxaga-Lerma, D.S. Balint, D. Dini, D.E. Eakins, A.P. Sutton, Attenuation of the dynamic yield point of shocked aluminum using elastodynamic simulations of dislocation dynamics, Phys. Rev. Lett. 114 (17) (2015) 174301.

[13] Y. Cui, G. Po, Y.P. Pellegrini, M. Lazar, N. Ghoniem, Computational 3-dimensional dislocation elastodynamics, J. Mech. Phys. Solids 126 (2019) 20–51.

[14] E. Van der Giessen, A. Needleman, Discrete dislocation plasticity: A simple planar model, Modelling Simul. Mater. Sci. Eng. 3 (5) (1995) 689.

[15] J.A. El-Awady, S.B. Biner, N.M. Ghoniem, A self-consistent boundary element, parametric dislocation dynamics formulation of plastic flow in finite volumes, J. Mech. Phys. Solids 56 (5) (2008) 2019–2035.

[16] O.C. Zienkiewicz, R.L. Taylor, The Finite Element Method for Solid and Structural Mechanics, Elsevier, 2005.

[17] J. Achenbach, Wave Propagation in Elastic Solids, Elsevier, 2012.

[18] J.M. Lees, Elastic Wave Propagation and Generation in Seismology, Wiley Online Library, 2003.

[19] G. Po, M. Lazar, N.C. Admal, N. Ghoniem, A non-singular theory of dislocations in anisotropic crystals, Int. J. Plast. 103 (2018) 1–22.

[20] A.M. Hussein, S.I. Rao, M.D. Uchic, D.M. Dimiduk, J.A. El-Awady, Microstructurally based cross-slip mechanisms and their effects on dislocation microstructure evolution in fcc crystals, Acta Mater. 85 (2015) 180–190.

[21] A.M. Hussein, J.A. El-Awady, Surface roughness evolution during early stages of mechanical cyclic loading, Int. J. Fatigue 87 (2016) 339–350.

[22] A.P. Thompson, H.M. Aktulga, R. Berger, D.S. Bolintineanu, W.M. Brown, P.S. Crozier, P.J. in't Veld, A. Kohlmeyer, S.G. Moore, T.D. Nguyen, et al., LAMMPS-A flexible simulation tool for particle-based materials modeling at the atomic, meso, and continuum scales, Comput. Phys. Comm. 271 (2022) 108171.

[23] Y. Mishin, D. Farkas, M. Mehl, D. Papaconstantopoulos, Interatomic potentials for monoatomic metals from experimental data and ab initio calculations, Phys. Rev. B 59 (5) (1999) 3393.

[24] J. Verschueren, B. Gurrutxaga-Lerma, D. Balint, D. Dini, A. Sutton, The injection of a screw dislocation into a crystal: Atomistics vs. continuum elastodynamics, J. Mech. Phys. Solids 98 (2017) 366–389.

[25] N.M. Ghoniem, L.Z. Sun, Fast-sum method for the elastic field of three-dimensional dislocation ensembles, Phys. Rev. B 60 (1999) 128–140, http://dx.doi.org/10.1103/PhysRevB.60.128, URL https://link.aps.org/doi/10.1103/PhysRevB.60.128.

[26] N. Ghoniem, M., S.H. Tong, L. Sun, Parametric dislocation dynamics: A thermodynamics-based approach to investigations of mesoscopic plastic deformation, Phys. Rev. B 61 (2) (2000) 913.

[27] L.P. Kubin, G. Canova, M. Condat, B. Devincre, V. Pontikis, Y. Bréchet, Dislocation microstructures and plastic flow: A 3D simulation, in: Solid State Phenom., 23, Trans Tech Publ, 1992, pp. 455–472.

[28] H.M. Zbib, M. Rhee, J.P. Hirth, On plastic deformation and the dynamics of 3D dislocations, Int. J. Mech. Sci. 40 (2–3) (1998) 113–127.

[29] W. Cai, A. Arsenlis, C.R. Weinberger, V.V. Bulatov, A non-singular continuum theory of dislocations, J. Mech. Phys. Solids 54 (3) (2006) 561–587.